Effects of Numerics on the Physics in a Third-Generation Wind-Wave Model

HENDRIK L. TOLMAN

Laboratory for Oceans, NASA/Goddard Space Flight Center, Greenbelt, Maryland

(Manuscript received 5 July 1991, in final form 3 October 1991)

ABSTRACT

Numerical errors in third-generation ocean wave models can result in a misinterpretation of the physics in the model. Using idealized situations, it is shown that numerical errors significantly influence the initial growth, the response of wave fields to turning winds, the scaling behavior of model results with wind speed, and the propagation of swell. Furthermore, the numerics may influence the dynamic interaction between wind sea and swell. Surprisingly, fetch-limited model behavior is hardly influenced by numerical errors in wave propagation. Simple modifications of the numerics are presented to reduce or eliminate such errors. The impact of numerical improvements for realistic conditions is illustrated by performing hindcasts for the Atlantic basin and for a smaller region off the east coast of the United States.

1. Introduction

In the last decades wind-wave models have undergone major development. Since the pioneering papers by Gelci et al. (1956, 1957), many wave models have been developed (e.g., SWAMP Group 1985, SWIM Group 1985). Presently the most advanced type of wave model is the so-called third-generation model (e.g., WAMDI Group 1988), which uses first principles in the integration of an action or energy balance equation. With the successful implementation of this model, the numerical wave model has become a powerful prediction and research tool for the systematic investigation of the dynamics of wind waves.

Recently, a research program has been initiated in which third-generation ocean wave models will be used in combination with a dense network of wave observations to improve our understanding of the physics of wave growth and decay [i.e., the Surface Wave Dynamics Experiment (SWADE), Weller et al. (1991)]. For the success of such a program it is essential to have detailed knowledge of the numerical accuracy of the model; numerical errors should not be attributed to physical processes and the magnitude of numerical errors determines the level of detail of the physics that can be assessed. To isolate numerical errors, other model errors related to input winds and parameterizations of the physics are considered to be beyond the scope of this study. The latter errors obviously attract the main attention within SWADE and will be discussed elsewhere.

The numerical model used in this study closely resembles the WAM model (WAMDI Group 1988), which was the first operational third-generation wave model. Since the WAM publication, more sophisticated (and more expensive) parameterizations for most source terms have become available. Such modified source terms are bound to have some influence on the numerics, but because the characteristics of the modified source terms must remain roughly identical in order for an overall wave energy balance to exist, the results of this study are expected to be fairly representative for most third-generation wave models.

In the present study numerical errors are analyzed using both idealized and realistic situations with an increasing degree of complexity. The first set of idealized situations considers time-limited growth for homogeneous conditions in order to isolate the numerics of source term integration from wave propagation. Second, numerical errors in swell propagation are briefly discussed considering pure propagation, and effects of numerical errors on the balance between propagation and source terms are investigated by considering fetch-limited growth. Finally, the impact of numerical errors and improvements for practical wave modeling is assessed by performing several hindcasts for the Atlantic basin grid and the regional grid of the SWADE experiment (Weller et al. 1991, Fig. 11).

2. Governing equations

The parameterizations of the physics of wind-wave propagation and generation used in this study are mainly taken from the first third-generation model WAM (WAMDI Group 1988). Henceforth, both this paper and the model will be denoted as WAM. A short

_____

Corresponding author address: Dr. Hendrik L. Tolman, NASA/ Goddard Space Center, Code 910.4, Greenbelt, MD 20771.

overview is given here for completeness only. For details reference is made to WAM.

Propagation and generation of ocean waves is described in WAM with a balance equation for the energy density spectrum $F(f, \theta)$, including a net source term $S(f, \theta)$:

$$\frac{\partial F}{\partial t} + (\cos\phi)^{-1} \frac{\partial}{\partial \phi} (c_\phi \cos\phi F)$$
$$+ \frac{\partial}{\partial \lambda} (c_\lambda F) + \frac{\partial}{\partial \theta} (c_\theta F) = S, \quad (1)$$

$$S = S_{in} + S_{nl} + S_{ds} + S_{bot}, \quad (2)$$

where f is the frequency and θ the direction of the spectral component, ϕ is the latitude, λ is the longitude, and c_ϕ, c_λ, and c_θ are the propagation velocities in the corresponding spaces (see WAM). For brevity of notation the dependence of F and S on f and θ has been omitted. The first term on the left side of Eq. (1) represents the local rate of change of the energy density. The second and third terms describe propagation in latitude and longitude, respectively, and the fourth term describes the change of wave direction due to great circle propagation and depth-induced refraction. In WAM the source term S [Eq. (2)] consists of (exponential) wind input S_{in} (Snyder et al. 1981), nonlinear wave–wave interactions S_{nl} (Hasselmann and Hasselmann 1985b), energy dissipation due to whitecapping S_{ds} (Komen et al. 1984), and energy dissipation due to bottom friction S_{bot} (Hasselmann et al. 1973).

The numerical implementation of Eqs. (1) and (2) is based on a discrete representation of all independent variables (ϕ, λ, f, and θ). It commonly features a fractional step method in which propagation and generation are treated separately. The numerical treatment of propagation is relatively straightforward; it corresponds to the well-known problem of multidimensional advection. Numerical schemes to solve these problems will be discussed later. The numerical treatment of the source terms (and the explicit calculation of S_{nl}) is typical for third-generation wave models and will be discussed briefly here.

WAM utilizes a semi-implicit time integration scheme to calculate the change of energy density ΔF in the time step Δt from the source terms S:

$$\Delta F(f, \theta) = \frac{S(f, \theta)}{1 - 0.5D(f, \theta)\Delta t} \Delta t, \quad (3)$$

where D is determined by the source terms [$D = \Lambda + \beta$, WAM Eqs. (4.1) through (4.10)]. This change of energy density per time step $\Delta F(f, \theta)$ is limited for each discrete spectral component ("bin") to a fraction ($\sim 10\%$) of the highest spectral level to be reached [estimated as the Pierson–Moskowitz level (Pierson and Moskowitz 1964)]:

$$\max(|\Delta F(f, \theta)|) = \Delta F_{max}(f) = 10^{-3}\pi c_g^{-1}k^{-3}. \quad (4)$$

After the change of energy density has been added to the (propagated) spectra, a parametric tail is applied for frequencies higher than f_{hf}. This cutoff frequency is based on both the wind speed (through the Pierson–Moskowitz frequency f_{PM}, i.e., the equilibrium frequency for fully developed sea state according to Pierson and Moskowitz 1964) and the mean frequency $\bar{f}$:

$$F(f, \theta) = F(f_{hf}, \theta) \left(\frac{f}{f_{hf}}\right)^{-m} \quad \text{for} \quad f > f_{hf}, \quad (5)$$

$$f_{hf} = \min[f_{max}, \max(2.5 \bar{f}, 4 f_{PM})], \quad (6)$$

$$f_{PM} \approx \frac{1}{2\pi} \frac{g}{28U_*}, \quad (7)$$

$$U_* = U_{10}\sqrt{(0.8 + 0.065U_{10})10^{-3}}, \quad (8)$$

where f_{max} is the highest discrete frequency, U_* is the wind friction velocity, and m is a constant (in WAM $m = 4$). The mean frequency $\bar{f}$ is a straightforward average over the spectrum. For an arbitrary parameter z the spectral average is given as

$$\bar{z} = E^{-1} \int_0^{2\pi} \int_0^\infty z(f, \theta)F(f, \theta)df d\theta,$$

$$E = \int_0^{2\pi} \int_0^\infty F(f, \theta) df d\theta. \quad (9)$$

In WAM the spectrum is usually described using 25 frequencies with a logarithmic frequency distribution ($f_{i+1} = 1.1 f_i$), with frequencies ranging from 0.042 Hz through 0.41 Hz. Furthermore, 24 directions are commonly used, resulting in a directional increment of $\Delta\theta = 15°$. This spectral resolution will be denoted as the standard spectral discretization. The preceding integration method for source terms shows stable behavior for time steps up to 20 min.

All calculations presented in this paper have been performed with a recent version of the model WAVEWATCH (Tolman 1991). The model version at the start of this study differs slightly from WAM in three ways. First, WAVEWATCH basically solves an action conservation equation to account for effects of mean currents; however, its governing equations reduce to Eq. (1) in the absence of currents. Second, in WAVEWATCH the bottom friction S_{bot} is modeled using a formulation of Madsen et al. (1988). For this study, this only influences results for the regional SWADE grid slightly. Finally, WAM uses $m = 4$ in Eq. (5). In this study, however, $m = 4.5$ has been used (unless specified differently) because it results in smoother numerical behavior in the dynamic integration schemes introduced in the following. Note that using physical arguments, it can be shown that the constant m should have a value between 4 and 5 (e.g., Phillips 1985). Furthermore, the use of $m = 4.5$ has been suggested before to make a local balance between the present

source terms at high frequencies possible (J. A. Greenwood, personal communication).

Finally, one addition is made to the physics of the model: for some idealized cases a linear growth term $S_{in,l}$ has been added to the source terms (2), to allow for the model to start without initial wave energy. The linear growth is described using a formulation of Cavaleri and Malanotte-Rizzoli (1981), where contributions for frequencies lower than f_{PM} have been eliminated:

$$S_{in,l}(f, \theta) = 1.5 \times 10^{-5} g^{-2}$$
$$\times \{ U_* \max[0, \cos(\theta - \theta_w)] \}^4$$
$$\times \exp\left[-\left(\frac{f}{f_{PM}} \right)^{-4} \right]. \quad (10)$$

The filter for low frequencies is added to $S_{in,l}$ to ensure that the range of the discrete frequency grid to low frequencies does not influence mean wave parameters at initial growth and hence initial growth itself. Because initial growth takes place at high frequencies, such a dependency on the low-frequency extent of a discrete frequency grid would be artificial. Note that this source term is relevant only for truly initial growth, because it is several orders of magnitude smaller than S_{in} for well-developed seas. This was confirmed by all numerical experiments including $S_{in,l}$.

3. Growth in homogeneous conditions

Homogeneous deep-water conditions have been considered first to separate the integration of source terms from propagation. In this case the energy balance equation (1) becomes

$$\frac{\partial F}{\partial t} = S_{in,l} + S_{in} + S_{nl} + S_{ds}. \quad (11)$$

A linear source term has been added to the right side of Eq. (11) to allow calculations to start without initial wave energy. Thus, no artificial initial conditions are needed. Deep water is considered so that the bottom friction source term S_{bot} can be omitted. The main attention will be focused on the mean frequency $\bar{f}$ [cf. Eq. (9)] and the significant wave height H_s:

$$H_s = 4\sqrt{E}. \quad (12)$$

For an intercomparison of results obtained with different wind speeds, a nondimensional time $\tilde{t}$, frequency $\tilde{f}$, and energy $\tilde{E}$ are used:

$$\tilde{t} = gt/U_*, \quad \tilde{f} = \bar{f}U_*/g, \quad \tilde{E} = g^2E/U_*^4. \quad (13)$$

Experiments based on Eq. (11) consist of three parts. First, the effect of the discrete time step, the spectral discretization, and the different frequency cutoffs will be assessed by considering growth curves for a constant wind speed. After that, scaling behavior will be assessed by comparing nondimensional growth curves for dif-

ferent wind speeds. Finally, the effect of numerical errors in more realistic but still artificial (homogeneous) conditions is assessed by considering variations in wind speed and direction as might occur during a rapid frontal passage.

a. Effects of the time discretization

The discrete time step Δt can influence numerical errors in two ways. First, discretization errors increase with increasing time step. Second, the limitation of the change of the spectral density per time step [Eq. (4)] will have an increasing effect with increasing magnitude of the time step. In Fig. 1, wave heights and mean frequencies for $U_{10} = 20$ m s^{-1} are presented as calculated with the implicit integration scheme and time steps Δt of 15 min, 5 min, and 5 s. Results obtained with the extremely small time step of 5 s can be regarded as free of numerical errors due to the discrete time step (obviously other numerical errors due to, for instance, the spectral discretization might still be present). Results obtained with time steps of 5 min and 15 min eventually converge to the "exact" results, as expected, because the equilibrium state should be stationary and therefore independent of the discrete time step. For initial growth, however, a larger time step reduces the wave height and increases the mean frequency.

To eliminate most time-step–related errors, time steps of 1 to 3 min appear necessary. The use of such small time steps would increase the computational costs of a model by an order of magnitude compared to conventional time steps of 15 or 20 min, whereas the increased time resolution is only needed for situations with rapid wave growth (or decay). In reality, these conditions can only occur locally and for a limited time. A more elegant solution would be to dynamically adjust the time step for source term integration, using small time steps in situations with rapid changes in the spectrum and larger time steps in near-equilibrium conditions. Note that rapid growth occurs only if the time scales associated with changes in the wind speed are smaller than the time scales of wave growth. Due to the limited resolution of wind fields in wave models such conditions occur for relatively strong winds, whereas spectra for low wind speeds are expected to remain near to equilibrium. Consequently, small time steps will mainly be needed for relatively strong winds.

Integration of source terms with a dynamically adjusted time step can be performed using the following fractional step method, which advances the solution over a period Δt in time. First, the entire wave field is propagated for a fixed time step Δt. The propagated solution is used as the starting point of the source term integration, which is performed for a number of dynamic time steps Δt_d until $\Sigma \Delta t_d = \Delta t$ (recalculating source terms each time step). The time step Δt_d is calculated for every grid point separately, because source terms at different grid points are essentially uncoupled.
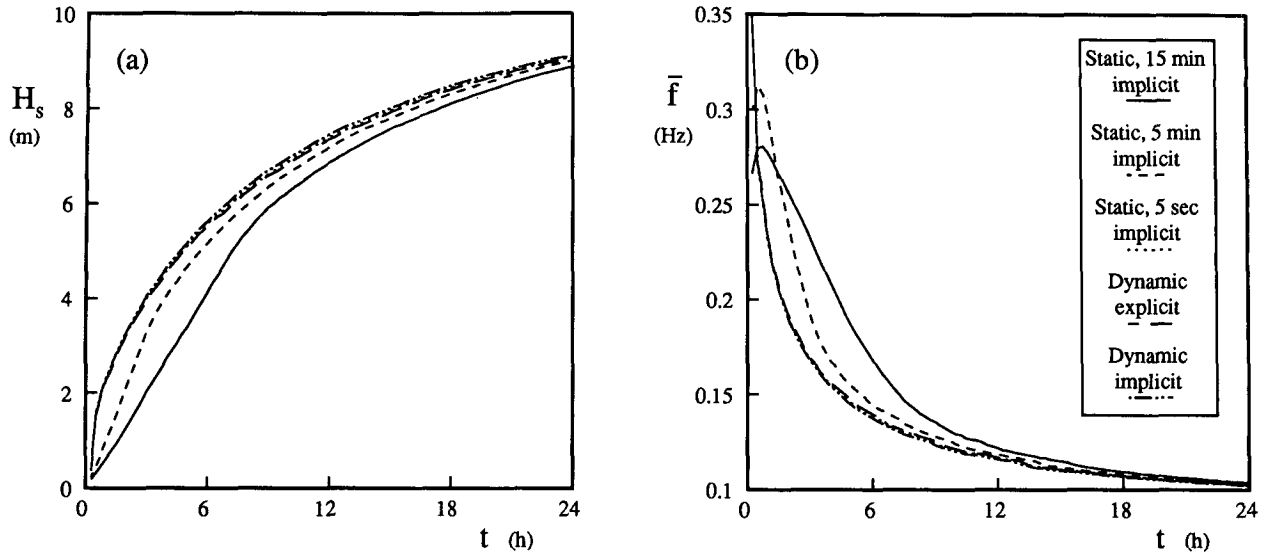
FIG. 1. The significant wave height H_s (a) and the mean frequency $\bar{f}$ (b) as a function of time t for several integration methods and time steps Δt (wind speed $U_{10} = 20$ m s^{-1}).

Thus, the time step for source term integration is reduced for selected grid points only. Henceforth, schemes with dynamically adjusted time steps for source term integration will be denoted as dynamic schemes, and schemes with a fixed time step as static schemes.

A simple way to determine a dynamic time step is to choose the time step so that the maximum change of energy density per spectral bin does not exceed a given fraction of some equilibrium energy level; in other words, the time step is chosen to satisfy limitation (4). Combined with a simple explicit integration scheme [i.e., Eq. (3) with $D \equiv 0$], dynamic integration is performed as

$$\Delta t_d^j = \min\left[\Delta t - \sum_{i=1}^{j-1} \Delta t_d^i, \min_{\substack{\forall \theta \\ f < f_{hf}}}\left(\frac{\Delta F_{\max}(f)}{|S(f, \theta)|}\right)^j\right], \quad (14)$$

$$F(f, \theta)^j = \max[0, F(f, \theta)^{j-1} + (S(f, \theta)\Delta t_d)^j], \quad (15)$$

where j is a local counter for the dynamic time step, set to 1 at the beginning of the integration for the grid point and the time interval Δt considered. Here $F(f, \theta)^0$ is the propagated energy density spectrum and $\Delta t_d^0 = 0$. The net source term $S(f, \theta)^j$ is calculated from the spectrum $F(f, \theta)^{j-1}$ at the beginning of the dynamic time step. At the end of the dynamic integration (i.e., when $\sum \Delta t_d = \Delta t$), $F(f, \theta)^j$ is the local solution at the new time level. Note that a more elaborate explicit dynamic scheme has been used before in the one-dimensional research model EXACT-NL (Hasselmann and Hasselmann 1985a; Van Vledder and Weber 1988).

The semi-implicit integration scheme of WAM can also be used as a basis of a dynamic scheme, in which case the dynamic time step (14) and the integration (15) become

$$\Delta t_d^j = \min\left\{\Delta t - \sum_{i-0}^{j-1} \Delta t_d^i, \min_{\substack{\forall \theta \\ f < f_{hf}}}\left[\frac{\Delta F_{\max}(f)}{|S(f, \theta)|}\right.\right.$$

$$\left.\left.\times \left(1 + 0.5\, D(f, \theta)\frac{\Delta F_{\max}(f)}{|S(f, \theta)|}\right)^{-1}\right]^j\right\}, \quad (16)$$

$$F(f, \theta)^j = \max\left[0, F(f, \theta)^{j-1}\right.$$

$$\left. + \left(\frac{S(f, \theta)\Delta t_d}{1 - 0.5\, D(f, \theta)\Delta t_d}\right)^j\right]. \quad (17)$$

Note that for initial growth the spectral densities F and hence the source terms S are extremely small. Consequently, the preceding schemes will not result in the expected small dynamic time steps. Therefore, the dynamic time step is forced to 5 s for extremely small nondimensional energies $\tilde{E} < 2.5$. For $U_{10} = 20$ m s^{-1}, this corresponds to a wave height of only 0.54 m. In realistic conditions this forcing of the dynamic time step is probably never used, since nondimensional energies are usually an order of magnitude larger than the limit value used here.

Results obtained with both the explicit and the implicit dynamic scheme with a time step $\Delta t = 15$ min are presented in Fig. 1 together with the previously discussed results of the static implicit scheme. This figure shows that the implicit dynamic scheme results in somewhat larger waves than the explicit dynamic

scheme, but for all practical purposes the results of the two schemes are identical to the results of the static scheme with a time step of 5 s. The increase in computational effort for the dynamic schemes compared to the conventional semi-implicit scheme with $\Delta t = 15$ min will be discussed later in the one-dimensional frontal passage case.

b. Effects of the spectral discretization

The spectral discretization generates numerical errors due to the resolutions $\Delta\theta$ and Δf (or $\Delta f/f$) in the direction and frequency spaces, respectively, and due to the finite range of the discrete frequency space. For homogeneous conditions with a wind speed $U_{10} = 20$ m s^{-1} such errors appear to be small; a reduction of either $\Delta\theta$ or Δf by a factor of 2 results in systematic variations of H_s and $\bar{f}$ of 1% or less. Adding discrete frequencies beyond the lowest discrete frequency of the standard spectral discretization has no effect on results (which was expected since the spectrum never reaches the lowest discrete frequencies), whereas adding higher frequencies influences the initial growth slightly, but has negligible effects after 6 to 12 h. Consequently, the standard frequency range appears to be adequate for a wind speed $U_{10} = 20$ m s^{-1}. Note that the frequency range is not necessarily adequate for other wind speeds.

c. Effects of the parametric tail

The choice of the constants in the cutoff frequency f_{hf} of (6) and the power m of the high-frequency tail influence the results. An increase of the constant for the mean frequency from 2.5 to 3.5 or an increase of the constant for the wind frequency f_{PM} from 4 to 5 both result in a decrease of H_s of 3% and an increase of $\bar{f}$ of 5% ($\Delta t = 5$ s, explicit integration for 48 h). Changing the power m of the parametric tail (5) from 4 to 5 (which is usually assumed to be a reasonable range for m) results in an increase of H_s of 5% and a decrease of $\bar{f}$ of 10%. This is astonishing considering that the tail contains a small part of the total energy within the spectrum. However, because the tail parameterization is more related to the physics than to the numerics, it is outside the scope of this study.

d. Scaling behavior

To compare growth characteristics for various wind speeds, calculations have been performed for wind speeds U_{10} of 5, 10, 15, 20, 25, and 30 m s^{-1} (static integration, $\Delta t = 5$ s). Because the wind speed U_{10} (or the friction velocity U_*) is the only external forcing, growth curves are expected to scale with the wind speed (friction velocity). Hence, the model should produce a single set of nondimensional growth curves. If the frequency grid is scaled to obtain identical nondimensional discrete frequencies as in (13), nondimensional

growth curves for all wind speeds indeed are identical (figure not presented here). However, if the standard spectral discretization is used (24 directions, 25 frequencies ranging from 0.042 Hz through 0.41 Hz), nondimensional growth curves for different wind speeds show large differences as is illustrated in Fig. 2. Growth curves for wind speeds of 15, 20, and 25 m s^{-1} show reasonable agreement with the results for scaled frequency grids. For 30 m s^{-1} they deviate from the above curves for times larger than 0.6×10^6. For wind speeds smaller than 15 m s^{-1}, they deviate extremely. This nonscaling behavior has to be related to the fixed (nonscaling) range of the frequency grid, but not to its resolution, because the logarithmic frequency distributions causes the frequency resolution to automatically scale with wind speeds. For high wind speeds, the limitation of the fixed frequency grid has been common knowledge in the WAM group; if waves keep growing, the spectrum eventually reaches the lowest discrete frequency and growth stops. In Fig. 2 growth for 30 m s^{-1} winds indeed stops around time 10^6. For lower wind speeds (5 and 10 m s^{-1}), the nonscaling behavior is less well known, but has a similar origin. For these wind speeds the wave spectrum is located at high frequencies, (partially) outside the discrete frequency range. Consequently, it is unlikely that the model shows good scaling behavior for these low wind speeds.

Considering the foregoing, the standard spectral discretization results in good scaling behavior for wind speeds between approximately 15 and 25 m s^{-1}. Because wind speeds are commonly much lower, the range of wind speeds with good scaling behavior should be extended to lower wind speeds by extending the discrete frequency range to higher frequencies. A measure for the highest discrete frequency (f_{max}) needed for a given wind speed can be obtained from scaling laws. To ensure that scaling behavior is adequate, the cutoff frequency f_{hf} [Eq. (6)] has to be within the discrete frequency grid ($f_{hf} < f_{max}$), because the actual highest frequency then becomes immaterial for both source team calculation and integration. In the final growth stages $f_{hf} = 4 f_{PM}$. For f_{hf} then to be within the discrete frequency grid, scaling laws result in the following constraint for the highest discrete frequency f_{max}:

$$f_{max} \geq 4 f_{PM} = \frac{4}{2\pi} \frac{g}{28 U_*}. \qquad (18)$$

Using this constraint, good scaling behavior is guaranteed for the final stages of growth, but not for all growth stages. Initial growth is described adequately only if the high-frequency range includes the spectrum in its first stage of growth. The highest discrete frequency needed to comply with this constraint can be estimated empirically from scaling laws, assuming that a given highest frequency is sufficient for a given wind speed (e.g., assuming that $f_{max} = 0.41$ Hz as in the
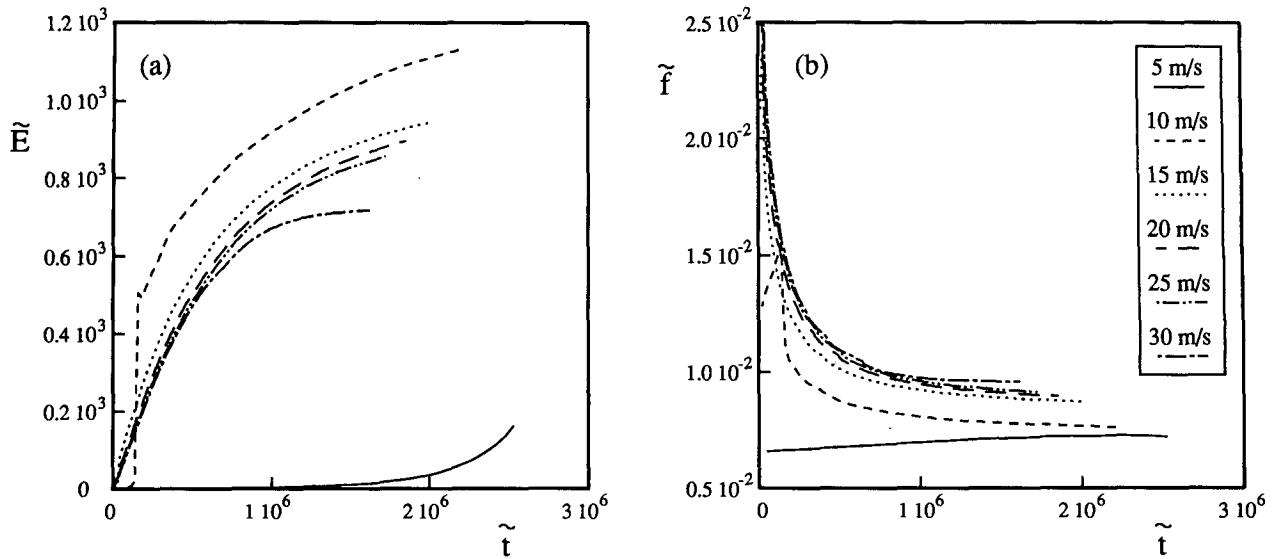
FIG. 2. (a) Nondimensional energy $\tilde{E}$ and (b) frequency $\tilde{f}$ as a function of nondimensional time $\tilde{t}$ for several wind speeds U_{10}. Time step $\Delta t = 5$ s, standard spectral discretization with 24 directions and 25 frequencies (0.042–0.41 Hz).

standard discretization is sufficient to describe initial growth for $U_{10} = 15$ m s^{-1})

$$f_{max} \geq f_{max,r} \frac{U_{*,r}}{U_*},\qquad(19)$$

where the suffix r refers to the above empirical reference conditions. Both constraints are illustrated in Fig. 3. Note that for low wind speeds the first constraint is especially important; wave conditions for these wind speeds are usually near full development due to the small time scales of wave growth. Such conditions have to be described well, since they represent "initial conditions" for storm cases. To illustrate the improved scaling behavior for an extended frequency range, growth curves obtained with 37 frequencies ranging from 0.031 to 0.97 Hz (i.e., three additional low and nine additional high frequencies) are presented in Fig. 4. Based on Fig. 3, good scaling behavior is expected for wind speeds larger than 7 to 8 m s^{-1}, which is in agreement with the results presented in Fig. 4.

e. Unsteady wind conditions

To assess the effect of the suggested numerical improvements under more realistic wind and wave conditions, a case with an unsteady but homogenous wind field has been considered, using the standard spectral discretization with five discrete high frequencies added. The wind speeds represent an idealized front and are presented in Fig. 5a and Fig. 5c. After an initial period with relatively low wind speeds (10 m s^{-1}, 0–4 h) the front passes between 4 and 6 h. The front is represented by a sharp increase in wind speed and a change in wind direction of 90°. After the front passes the wind speed

and direction remain constant (6 to 12 h) and finally the wind speed reduces (12 to 18 h). Presented are the significant wave heights H_s (Fig. 5b) and mean directions $\bar{\theta}$ (Fig. 5c):

$$\bar{\theta} = \arctan\left[\frac{\int\int \sin\theta\, F(f, \theta)}{\int\int \cos\theta\, F(f, \theta)}\right].\qquad(20)$$
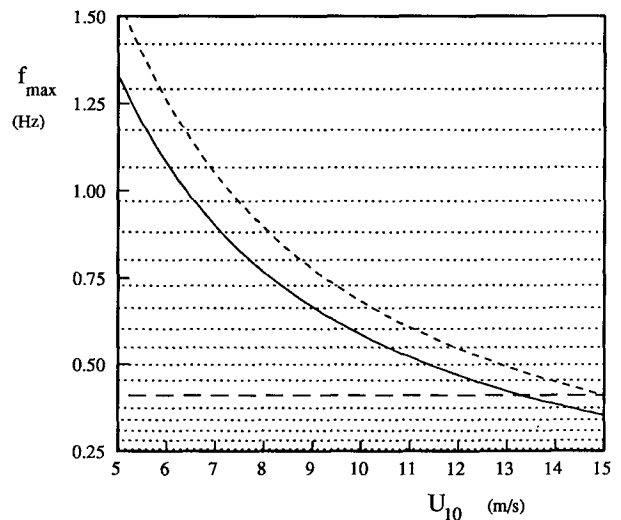

FIG. 3. Required maximum discrete spectral frequency f_{max} as a function of wind speed U_{10}. Solid line: requirement for convergence [Eq. (18)]. Dashed line: resolution compatible with standard spectral resolution for $U_{10} = 15$ m s^{-1} [Eq. (19)]. Long dash: conventional f_{max}. Dotted lines: discrete frequencies of the (extended) standard discretization.
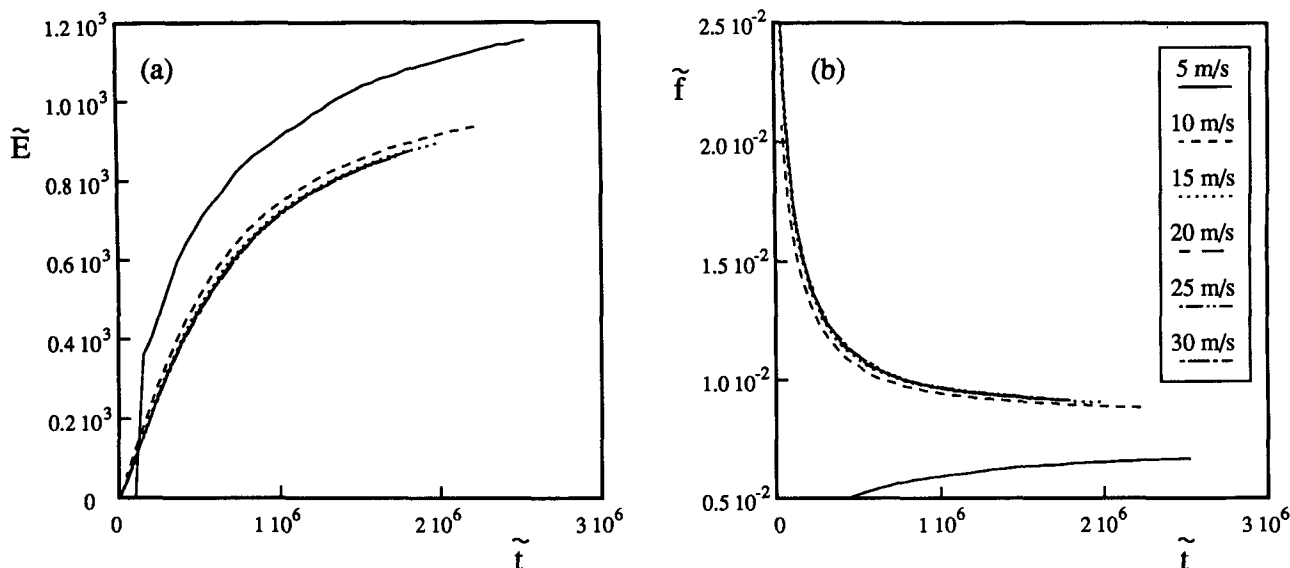
FIG. 4. Same as Fig. 2 except for spectral discretization (37 frequencies, 0.031–0.97 Hz).

Results for a implicit-static scheme with time steps of either 5 s (solution with negligible time-step errors) or 15 min (conventional), and with both the explicit and implicit dynamic scheme with a basic time step of 15 min, are presented in Fig. 5. The figure clearly shows the differences between the conventional time integration (dashed lines) and the "exact" solution (solid lines), in particular for the directions. During the frontal passage (i.e., between 4 and 6 h) the rate of change of direction ($\partial\theta/\partial t$) of the conventional approach (dashed line) is typically only half that of the exact solution (solid line). The results for the explicit-dynamic (long dash) and implicit-dynamic (dotted lines) schemes can hardly be distinguished from the solid lines (exact solution).

In Fig. 5d the number of dynamic time steps n_d per 15-min basic time step are presented for both dynamic schemes. The explicit scheme shows values of n_d of 10 to 15, corresponding to dynamic time steps $\Delta t_{d,\text{avg}} \approx \Delta t/n_{d,\text{avg}}$ of the order of 1 to 2 min. The implicit scheme allows for much larger dynamic time steps. For this case the average number of dynamic time steps $n_{d,\text{avg}} \approx 2.0$ ($\Delta t_{d,\text{avg}} \approx 7.5$ min), effectively doubling the computational effort compared to the conventional static approach. The major part of the extra computational effort is used during the actual frontal passage, where the dynamic time step of the implicit scheme is reduced to approximately 3 min. Because the implicit dynamic scheme is much cheaper than the explicit scheme and gives similar results for mean wave parameters, it appears to be preferable.

4. Propagation and fetch-limited growth

Wave propagation is important both for swell propagation and for fetch-limited growth. The former case

considers pure propagation with a negligible effect of source terms and the latter case considers the local balance between effects of propagation and wave growth.

Swell propagation is described by a well-known multidimensional advection equation. WAM uses either a first-order upwind ("upwave") propagation scheme or a second-order leapfrog scheme. The first-order scheme is commonly used and has many advantages: it is fast and simple and does not show artificial solutions (e.g., negative energy). Its disadvantage is the large numerical diffusion, making the scheme highly dissipative. Second-order schemes such as the leapfrog scheme reduce the numerical diffusion, but usually incorporate significant numerical dispersion. This results in artificial wavy solutions with negative energy near strong gradients. In WAM, this problem is solved by adding explicit diffusion to the leapfrog propagation scheme, making it essentially as dissipative as the first-order scheme (WAM, p. 1781). In the Crank–Nicolson scheme originally used in WAVE-WATCH, similar problems occur. Here, the scheme is mixed with a first-order scheme, also introducing some diffusion. Other solutions are available to eliminate the dispersion errors of second-order schemes without adding excessive diffusion/dissipation (e.g., see Fletcher 1988). In this study, the first-order scheme will be compared with a scheme based on the sharp and smooth transport algorithm (SHASTA, Boris and Book 1973, 1976; Book et al. 1975), which uses a flux-corrected transport (FCT) algorithm to assure physical behavior. The actual implementation of this scheme is discussed in the Appendix. The capability of this scheme to yield both small dissipation and dispersion errors is illustrated in Fig. 6, where a narrow cosine-like energy distribution on a background level has been
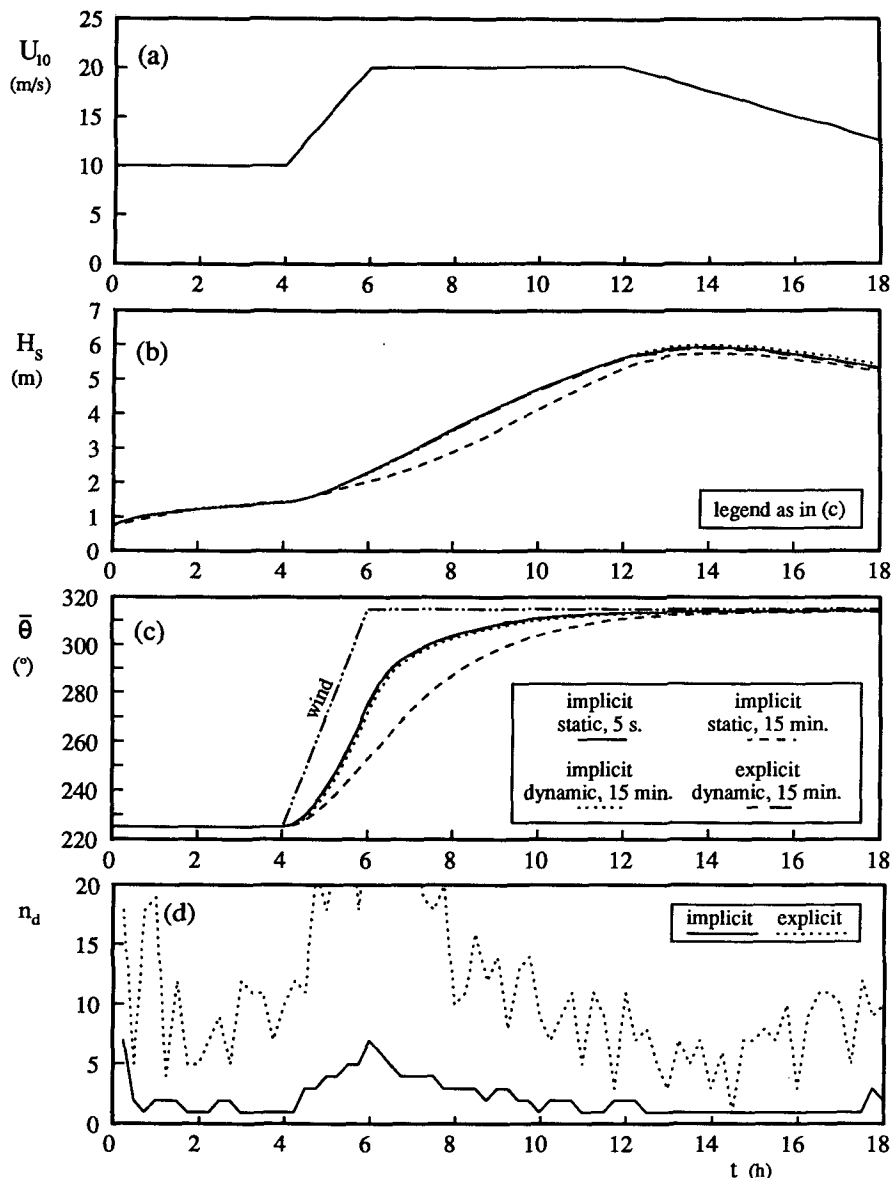
FIG. 5. Results for unsteady but homogeneous wind case resembling a strong frontal passage. (a) wind speed U_{10}, (b) significant wave height H_s, (c) mean wave direction $\bar{\theta}$, and (d) number of dynamical time steps per basic (15 min) time step n_d. Spectral discretization with 30 frequencies (0.042–0.66 Hz).

propagated for 100 time steps with a Courant number 0.281.

Fetch-limited growth is investigated by considering the following time-independent one-dimensional deep-water version of Eq. (1):

$$c_g \frac{\partial F}{\partial x} = S_{in,l} + S_{in} + S_{nl} + S_{ds}. \qquad (21)$$

All numerical experiments with this equation have been performed using the standard spectral resolution and a wind speed of 20 m s^{-1}. Grid increments Δx

and time steps Δt vary. To obtain the time-independent solution, a time-dependent version of (21), including a term $\partial F/\partial t$ at the left side, is solved until the results become steady. Again $S_{in,l}$ is used for initialization purposes only and again was found to have negligible effects on the final steady solution for the full spectral model.

In a numerical solution of (21) errors can occur due to the choice of the propagation scheme and due to the grid increment Δx. Errors in the source term integration are assumed to be negligible by considering sufficiently small time steps and sufficient spectral res-
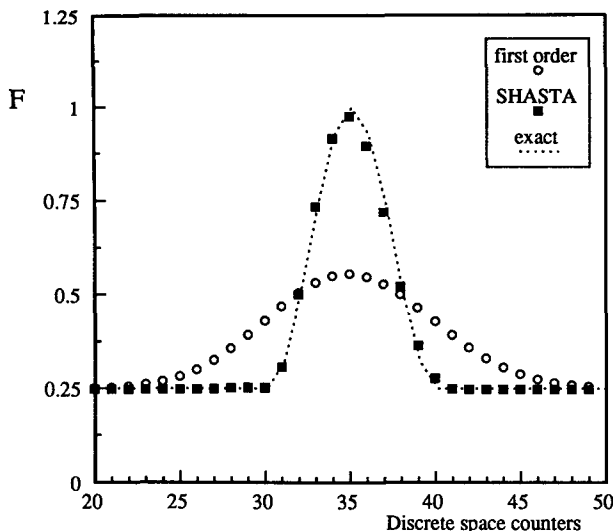
FIG. 6. One-dimensional deep-water propagation of a single spectral bin with first-order and SHASTA schemes. Propagation over 28.1 grid increments in 100 time steps (arbitrary energy units).

olution. The effect of the propagation scheme on fetch-limited behavior is studied by further reducing Eq. (21) to linear and exponential growth for one frequency and direction only:

$$c_g \frac{\partial F}{\partial x} = S_{in,l} + S_{in}, \qquad (22)$$

for which the analytical solution becomes

$$F(x) = \frac{S_{in,l}}{S_{in}} \left[\exp\left(\frac{S_{in}x}{c_g}\right) - 1 \right]. \qquad (23)$$

Using analytical solutions for the time integration of the source terms in (22) and forcing the fetch-unlimited solution to a saturation limit E_∞ by multiplying the source terms with a factor

$$r = 1 - \max\left[0, \left(\frac{E - 0.75E_\infty}{0.25E_\infty}\right) \right]^2, \qquad (24)$$

"growth curves" for both propagation schemes have been calculated. In Fig. 7 results are presented for a f = 0.1 Hz and the Pierson–Moskowitz saturation level on which (4) is based (Δx = 25 km, Δt = 15 min). The first-order scheme shows an overestimation of $F(x)$. This is caused by the upwind estimation of spatial gradients, which results in an underestimation of spatial gradients and therefore in an underestimation of propagation. Because source terms are calculated at the grid points and thus are "exact," the net effect is an overestimation of $F(x)$. The second-order scheme does not have this deficiency and shows near-perfect results.

From the results of Fig. 7, it is expected that the two schemes show different fetch-limited behavior for the full spectral form of Eq. (21). To investigate this, fetch-

limited calculations have been performed for both schemes (Δx = 25 km, Δt = 225 s). Surprisingly, wave heights and mean frequencies are practically identical for both schemes (see Fig. 8). After inspecting the results in detail, it appears that this behavior has two causes. First, both schemes use an identical upwind boundary treatment at x = 25 km and should therefore show identical results at this point. As will be shown later, a significant part of the numerical propagation error is concentrated in this point. Second, the first-order scheme smooths gradients in space, which slightly lowers spectral peaks. This slightly decreases nonlinear interactions and hence reduces growth rates, which compensates part of the diffusion error in propagation (figures not presented here).

The effect of the grid resolution can be assessed by considering fetch-limited growth curves for several resolutions in otherwise identical models and conditions. In Fig. 9 wave heights and mean frequencies are presented for grid resolutions of 6.25 km, 25 km, and 100 km (first-order scheme, Δt = 225 s). The largest grid increment is fairly representative for fine-resolution ocean wave modeling (e.g., the SWADE Atlantic basin models), whereas the smallest is roughly representative for detailed coastal models. Because results for the smallest increment Δx should have the smallest numerical errors, a finite increment appears to result in an overestimation of the wave height and an underestimation of the mean frequency. A major part of this error is generated in the first grid point. This is illustrated in Fig. 9 with results obtained with Δx = 25 km, using boundary conditions at x = 25 km from a run with resolution Δx = 6.25 km (i.e., a nested model where a significant part of the boundary error is removed). Since the results of the nested run (triangles)
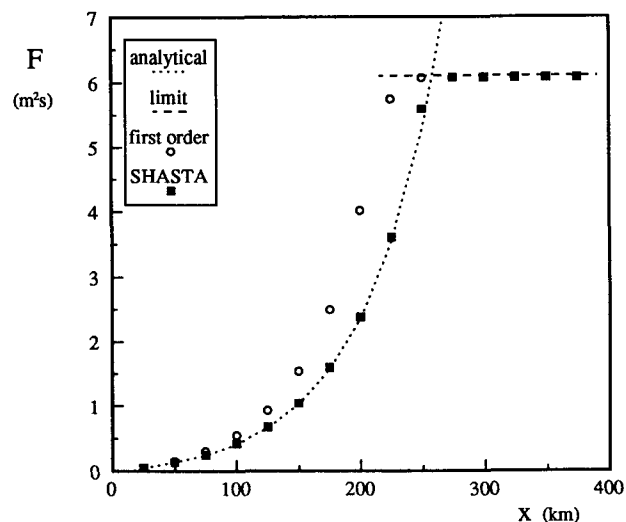

FIG. 7. Fetch-limited growth for a single frequency and direction due to linear and exponential growth and a limiting energy level. f = 0.1 Hz, U_{10} = 20 m s^{-1}, Δx = 25 km, and Δt = 15 min.
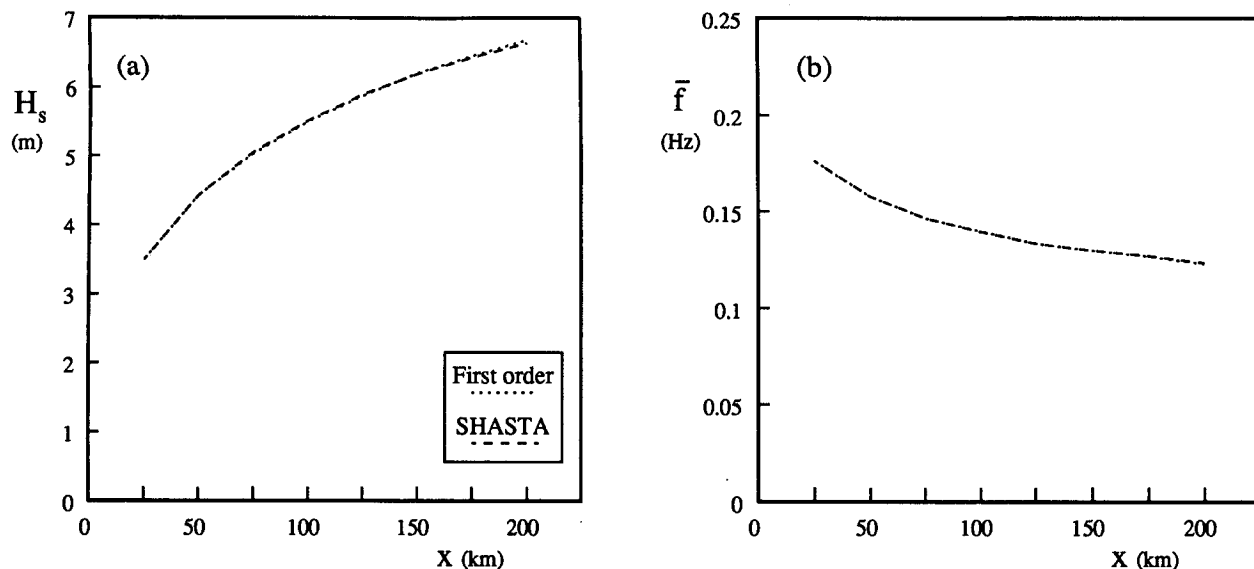
FIG. 8. Full-spectral fetch-limited growth curves of (a) the significant wave height and (b) the mean frequency for different propagation schemes. Wind speed 20 m s^{-1}, standard spectral discretization, $\Delta x = 25$ km and $\Delta t = 15$ min, dynamic implicit source term integration.

remain close to the results for high grid resolution (dotted line), it appears that the major part of the differences between the runs with different resolutions (and hence the numerical errors) arises in the first grid point. Note that repeated calculations with the second-order scheme (figures not presented here) show similar results, the impact of the change of resolution being much larger than the impact of the change of schemes.

Two remarks must be made on the results presented in this section. First, the effects of the grid discretization on fetch-limited growth depend on wind speed through scaling laws. The nondimensional grid increment $\Delta\tilde{x}$ is given as $\Delta\tilde{x} = g\Delta x/U_*^2$ (cf. the nondimensional fetch $\tilde{x}$). For an increasing increment Δx or a decreasing wind speed U_{10} (or U_*), the nondimensional grid increment increases. Consequently, the importance of the error at the first grid point becomes even larger than in the case considered here (which uses fairly high winds and small grid increments). Simultaneously, the effect of the propagation scheme becomes smaller. Sec-
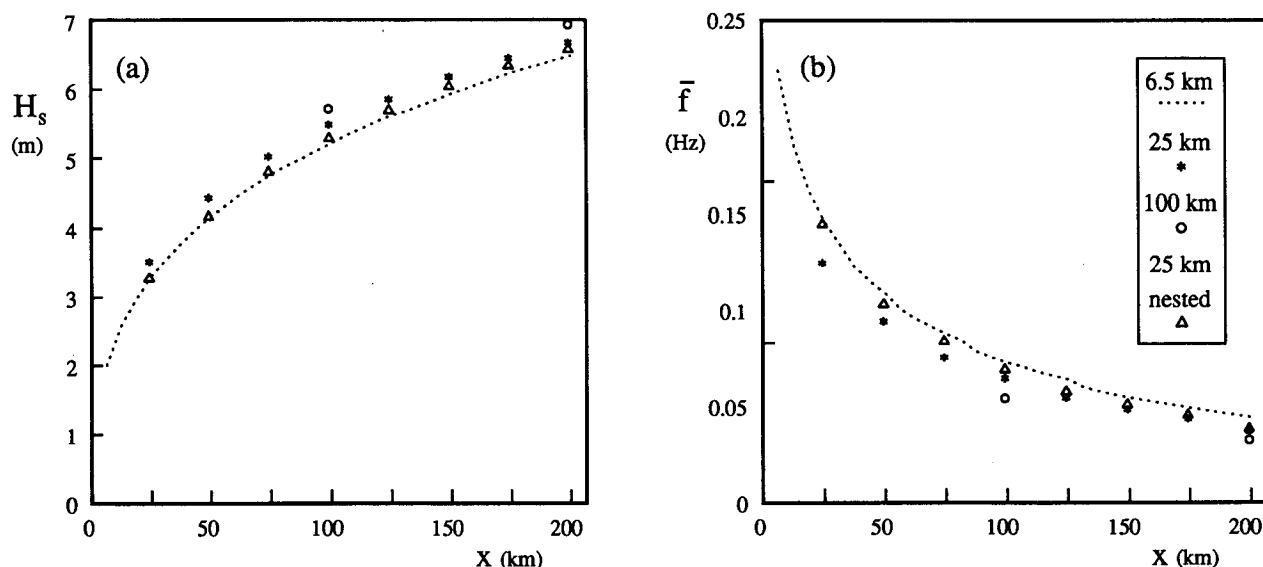

FIG. 9. Fetch-limited growth curves of (a) the significant wave height and (b) the mean frequency for several grid increments Δx. Wind speed 20 m s^{-1}, standard spectral discretization, $\Delta t = 225$ s, first-order scheme. The nested results are obtained using boundary conditions from the results for $\Delta x = 6.25$ km at $x = 25$ km.

ond, one might expect the overall results to be affected by the time step. However, repeated calculations with a much smaller time increment (30 s) and with dynamic schemes (using the maximum time step for stable propagation for the grid resolution considered) reproduce the time-independent results presented here closely.

5. The SWADE October storms

To investigate the impact of the preceding numerical improvements for realistic wave modeling, several hindcasts have been performed for two of the SWADE grids for the period of 22–29 October 1990 (including a model spinup period on 20–21 October). The grids cover the Atlantic Ocean and part of the east coast of the United States, respectively, and are denoted as the basin grid and the regional grid (see Weller et al. 1991, Figs. 11a and 11b). The resolution of the basin grid is $1° \times 1°$ and of the regional grid is $0.25° \times 0.25°$. The propagation time steps are 15 min and 10 min, respectively. Boundary conditions for the regional grid are obtained from the corresponding run on the basin grid. The wind fields for the basin grid consist of NMC operational global analysis wind fields (interpolated from the original $2.5° \times 2.5°$ grid), which are available every 6 hours. This time and space resolution is fairly representative for wind fields used for ocean-scale wave hind- and forecasting. The wind fields for the regional grid consist of an analysis on a 50 km $\times$ 50 km grid, which is also available every 6 hours. This analysis is specially developed for SWADE at NASA/Goddard Laboratory for Atmospheres and will be presented in detail elsewhere. The resulting regional wind fields are much more detailed in space than the basin-scale winds, but still poorly resolved in time. Note that within the model wind speeds are interpolated to obtain wind speeds central in time for each (propagation) time step considered.

Calculations have been performed with three different versions of the model. In the first version (denoted A), a conventional numerical approach is used [24 discrete directions, 25 frequencies (0.042–0.41 Hz); static, implicit source-term integration; first-order propagation scheme]. In the second version (B), the improvements for source-term integration have been incorporated; an extended frequency range (33 frequencies, 0.041–0.88 Hz) and dynamic, implicit source term integration are used. This frequency range assures good scaling behavior for wind speeds from approximately 7.5 m s^{-1} to 25 m s^{-1}. A first-order upwind propagation scheme is still used. In the third version (C), all improvements have been incorporated, including the second-order accurate SHASTA propagation scheme. In the following the effects of the improved source term integration is assessed by considering the difference in results of model versions A and B. Similarly, the difference between results of versions

B and C shows the effect of improved propagation and the differences between A and C show the total effect of numerical improvements. The model comparisons will concentrate of the significant wave height H_s (12) and the mean period T [= f^{-1}, cf. (9)].

a. Results for the basin grid

To illustrate the impact of numerical improvements on the basin hindcasts, significant wave heights and mean periods for 0000 UTC 26 October 1990 are presented in Fig. 10. Also presented are the differences induced by the numerical improvements (i.e., the differences between models C and A). The wave heights and periods (Fig. 10, panels a and b) show two large active storm systems, marked as A and B. System B has caught up with an old swell system traveling in roughly the same direction. Furthermore, two distinct swell systems (marked as C and D) can be distinguished. The structure and wave direction of the storm systems is clear from the figure. Swell system C travels in northeasterly directions and has been generated approximately two days earlier. Swell system D travels in southeasterly directions and has been generated four days earlier in the Labrador Sea (approximately 50°N, 55°W). Note that on top of swell system D, a newly generated wind sea travels in southwesterly directions.

The changes in wave height ΔH_s and periods and ΔT due to the improved numerics are presented in Fig. 10, panels (c) and (d), positive values corresponding to an increase due to the improved numerics. By animating the changes in wave height and period due to (part of the) numerical improvements, the following observations could be made.

First, the dynamic integration has little effect on the mean wave parameters ($n_{d,\mathrm{avg}} \approx 1.2$), as was expected, because the wind fields used here are fairly smooth both in space and time. However, the wave height shows small modulations with time scales of a few hours (not shown here). In fact, small-scale features of the wind fields can be distinguished in animations of ΔH_s and ΔT, particularly in the tropics. Such effects, however, cannot be distinguished in Fig. 10.

Second, the extended frequency range results in a systematic reduction of wave heights and periods for areas with low wind speeds. For high wind speeds, effects of the extended frequency range appear to be negligible. In Fig. 10 these effects can be recognized as a systematic reduction of T and H_s in the tropics (ΔT typically -1.75 s, ΔH_s typically -0.3 m), whereas in active generation areas mean wave parameters are only slightly influenced.

Third, the improved propagation scheme strongly influences the propagation of swell, increasing the wave height at the swell peak and reducing the spread of wave energy in the propagation direction. This spatial concentration of swell energy results in a similar variation of wave periods. In Fig. 10, panels (c) and (d),
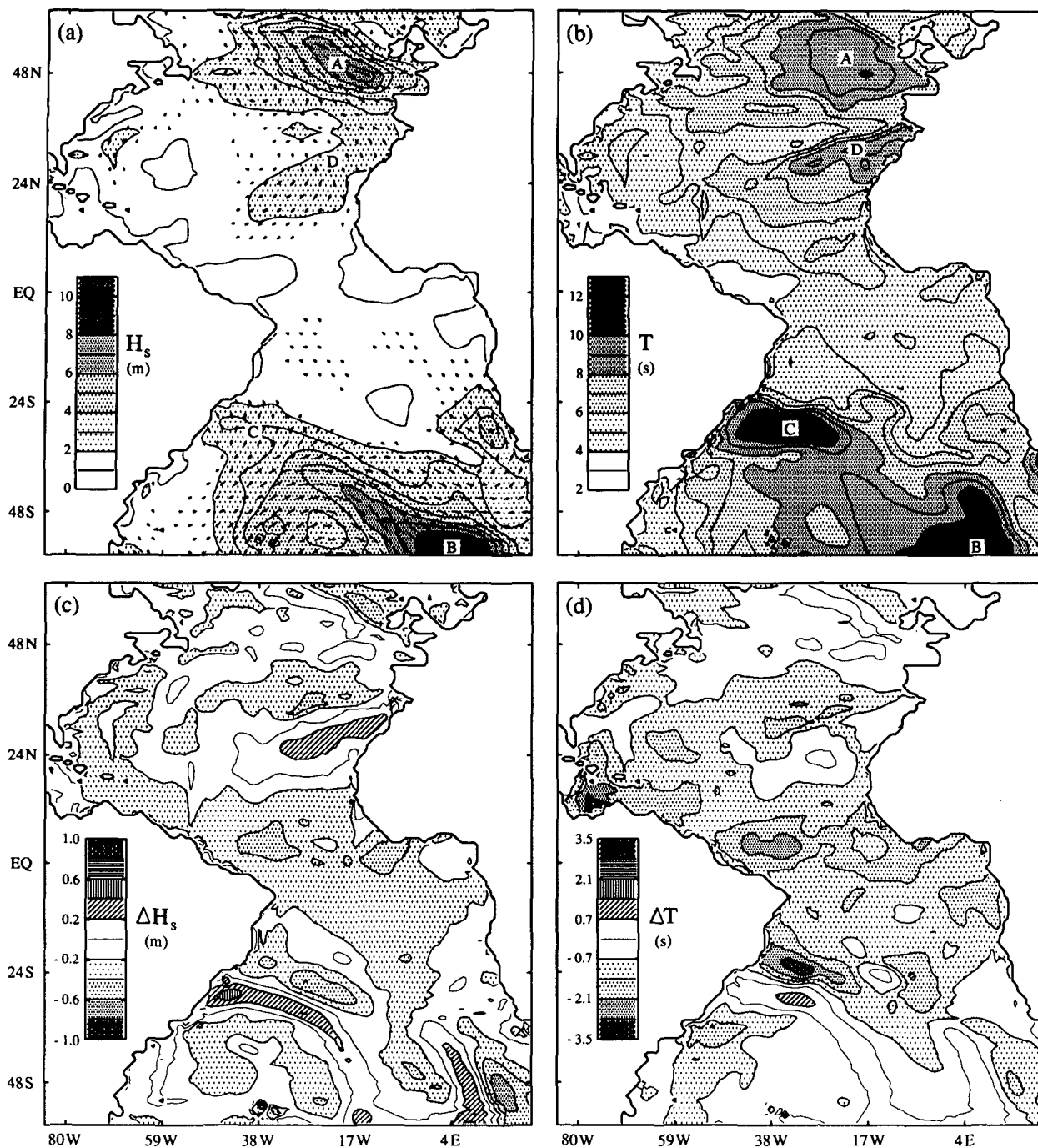
FIG. 10. Model results for the basin model at 0000 UTC 26 October 1990. (a) Significant wave height H_s and (b) the mean period T from the improved model. (c) Wave height variations ΔH_s and (d) mean period variations ΔT as induced by the numerical improvements. The arrows in panel (a) point in the mean wave propagation direction and their length is scaled with H_s.

the enhanced swell peak and the reduction of wave height and period in front of and behind the swell peaks can be observed clearly for the swell fields C and D, and for the old swell field in storm B.

Fourth, one might expect the numerical improvements to influence the dynamic interaction between swell and wind sea because (i) the extended frequency range will result in moderate wind–sea spectra at higher frequencies, with a larger frequency gap between swell and wind sea, (ii) the dynamic time integration might cause a more rapid growth of young wind sea, and (iii) the improved propagation schemes have a large impact

on the local swell energy. The different frequency gaps and magnitudes of swell and wind sea energy cause differences in the nonlinear interactions between the two fields. Furthermore, they influence the overall wave steepness and hence dissipation rates. One indication of a modified dynamic interaction between swell and wind sea can be found in swell field D in Fig. 10, which shows systematically enhanced wave heights due to source term improvements only (not shown here). This might be related to the aforementioned effects of an enhanced frequency range. The model output was not sufficient to investigate this process in detail. Another indication can be found at the boundaries of moving storm systems, where animation of ΔT regularly shows wave periods that are reduced by more than 3 s (in Fig. 10d, however, such regions are not observed). These reductions can be explained qualitatively from averaging over a spectrum with enhanced growth of wind sea and from reduced diffusive swell propagation out of the wind sea field. A comparison of results of all three model versions indicates that all numerical improvements play a significant role at the boundaries of storm systems.

b. Results for the regional grid

The regional model shows essentially the same effects of improved numerics as the basin model, except for two additions.

First, the enhanced spatial resolution of the wind fields results in higher maximum wind speeds and therefore in larger temporal variations of the wind, in spite of the large time interval over which new fields are available. With the more rapidly changing wind conditions, dynamic time integration becomes more important, even though the basic time step is smaller than in the basin model. For one small-scale storm this resulted in a significant increase of the wave heights (up to 1.5 m) as illustrated in Fig. 11b-d (i.e., wind sea at approximately 44°N 55°W). Such differences occur on relatively short time scales (typically 3-6 h).

Second, the regional bottom grid shows large variations on the continental shelf, with some shallow grid points near the shelf edge (Fig. 11a). At these shallow points, the dynamic time integration without a limit to the change of energy density per time step allows the bottom friction term to be much more active. This results in a clearer "imprint" of shallow grid points on wave heights and periods.

Finally, Fig. 12 shows wave heights, periods, and directions for the location of NDBC buoy 44004 (38°30'N, 70°36'W) as obtained with either the conventional approach (dotted lines) or with the improved numerics (solid lines). This figure illustrates the impact of the numerical modifications for mean wave parameters at a given point. The wave height (Fig. 12a) slightly decreases, in particular for lower wave heights. The mean period (Fig. 12b) shows a significant de-
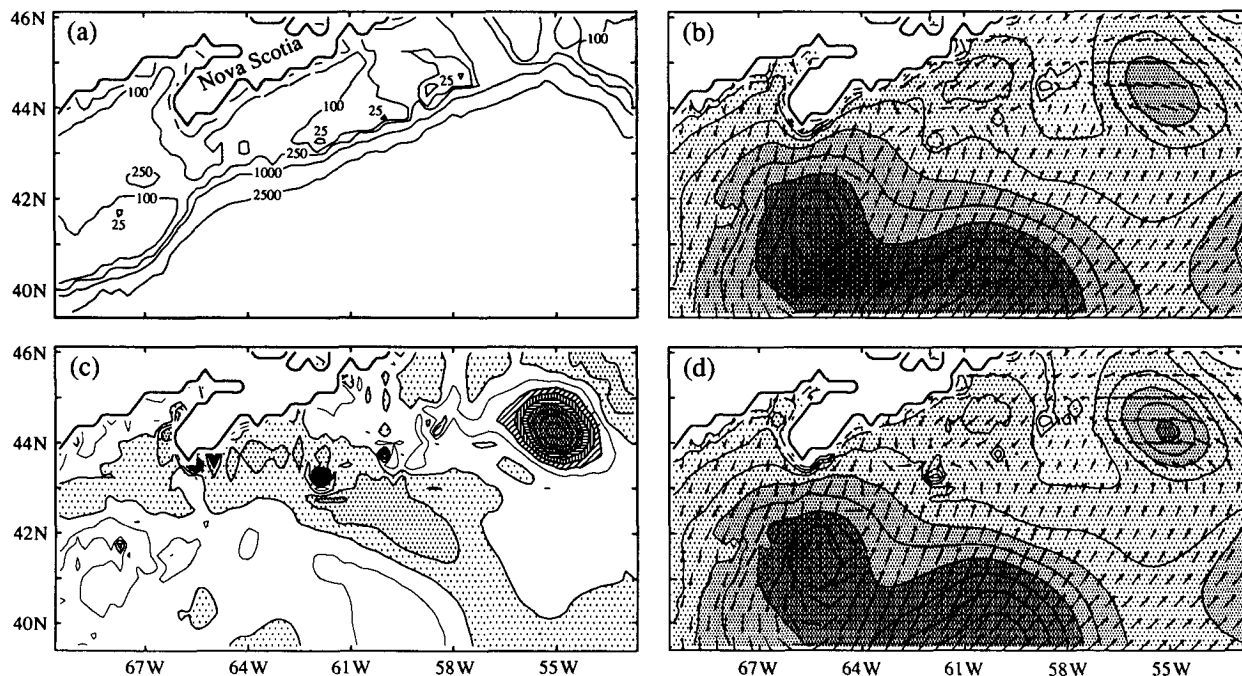

FIG. 11. Model results for part of the regional model at 1200 UTC 27 October 1990. (a) Water depths in meters, (b) significant wave height H_s for the conventional numerics, and (d) the improved numerics, and (c) the differences between both models. Legend as in Fig. 10.
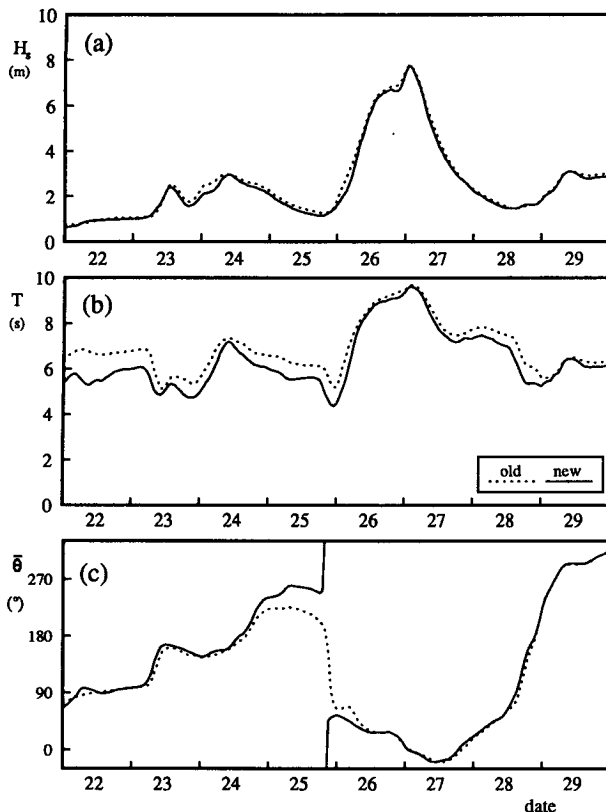
FIG. 12. Regional model results for the location of NDBC buoy 44004 (38°30'N, 70°36'W) in October 1990. Conventional numerics (dotted lines) and improved numerics (solid lines).

crease, again in particular for moderate wind and wave conditions. Finally, the mean wave direction becomes more sensitive to variations of wave (wind) conditions (in particular 22 and 23 October) and can show large systematic differences for low wind speeds (25 October).

6. Discussion

The idealized and realistic wave generation and propagation conditions considered in this study clearly show that the conventional numerical approach in third-generation wave models incorporates significant numerical errors. These errors can easily result in a misinterpretation of the physical behavior of such models. In particular, growth rates, response to turning winds, low wind speed conditions, and propagation of swell are influenced. Furthermore, the sharpness of spectra is slightly influenced and the dynamic interaction between swell and wind sea may be influenced. If a model is to be used as a research tool to investigate the details of wave dynamics, such errors should be eliminated, or at least rightfully attributed to numerics instead of physics. As is shown in this study, a significant part of the numerical errors can be eliminated in

a relatively simple way by using a dynamic integration of source terms, an extended frequency range, and more accurate propagation schemes.

In this study the dynamic time step has been related to a spectral equilibrium level only. This introduces several potential disadvantages. First, swell energy levels are, by nature, much smaller than the equilibrium level. Therefore, they are unlikely to influence the dynamic time step (except for extremely shallow water next to much deeper water as in the regional model). To assure accurate time integration of such spectral components, in particular in situations with significant bottom friction, the dynamic time step should also be related to, for example, the relative change of energy density (as in EXACT-NL). Furthermore, one might be able to make the dynamic integration more economical by modifying the dependence of ΔF_{max} on k and c_g and by maintaining static integration for wind speeds for which the chosen frequency range is expected to show poor scaling behavior, assuming that the latter results will show significant numerical errors anyhow. Another reason for maintaining static integration in the latter conditions is that unrealistic behavior of the nonlinear interactions is observed to occur, which can reduce dynamic time steps significantly. Finally, it should be noted that the dynamic integration is expected to become increasingly important, when wind fields with a better temporal resolution are considered.

The choice of the highest discrete frequency is essentially governed by economic considerations, as long as the highest discrete frequency is low enough for all source term parameterizations not to incorporate part of the capillary wave region. However, as important as increasing the frequency range is the way in which model results are analyzed. Such an analysis should obviously concentrate on wind speed ranges for which numerical errors related to the finite frequency range are expected to be small.

The literature concerning the solution of advection problems is vast and many different schemes have been used in wave models (e.g., SWAMP Group 1985). The scheme presented here has good properties for wave propagation, although across-grid propagation at high Courant numbers could be improved. Recently the interest in higher-order propagation schemes for wind wave models has increased (e.g., Neu and Won 1990), due to studies such as SWADE and the "Bight of Abaco" experiment.

The three improvements suggested here do not deal with all sources of numerical errors. In this study also the effect of a finite spatial resolution near coastlines has been recognized. This is, however, strongly related to the degree of spatial resolution that is economically feasible. A reduction of spatial resolution results in an increase of computational effort that roughly scales with the third power of the grid refinement, due to the two-dimensional grid and Courant limitations on the time step. Furthermore, swell propagation for discrete spec-

tra leads to a disintegration of a continuous wave field ("garden sprinkler effect," Booij and Holthuijsen 1987). When numerical diffusion is eliminated from the propagation schemes, such effects might become apparent in models. This error can be reduced greatly by applying controlled diffusion to the propagation equation and by increasing the directional resolution to $\Delta\theta \approx 5°$ (Booij and Holthuijsen 1987).

Even with all of the suggested numerical improvements, each model will have some numerical errors. For a complex wave model, the remaining numerical error is difficult to quantify. Assuming that the remaining numerical error is much smaller than the differences between the old and new approaches, numerical errors in wind-dominated conditions might be expected to be a few percent at most, except for situations where the high-frequency range of the discrete spectrum is insufficient. Swell propagation obviously remains sensitive to numerical errors due to the nature of the problem and the usually poor model resolutions. Perhaps more important than a well-defined estimate of remaining errors is the recognition by wave modelers engaged in basic research of wind wave physics that model errors can lead to a misinterpretation of results. The only practical way to assess this problem appears to be to perform duplicate calculations with modified numerics.

The hindcasts for the SWADE storms show that the new numerics systematically reduce wave heights and mean wave periods for low wind speeds (ΔH_s typically -0.3 m and ΔT typically -1.75 s, for the moment ignoring local, fluctuating effects of propagation errors on swell). For more extreme wind and wave conditions the effects of the new numerics are generally much smaller, whereas significant increases of H_s and T on small space and time scales could be realized with higher-resolution winds. This systematic variation of numerical errors with wind speed will change the slope of regression curves for observed and calculated wave data. Therefore, even the relatively small effects of numerics on wave heights might have a recognizable impact in model verification studies. The much larger effects of numerics on wave periods is bound to have a distinct effect in verification studies. However, the mean period is a convenient model parameter to compare due to its straightforward definition, but it is physically less relevant than, say, the peak period of the (wind sea part of the) spectrum. At low wind speeds the latter parameter is strongly influenced by the extent of the discrete frequency grid to high frequencies. Due to averaging over swell and wind seas, the mean wave period T will generally show smaller changes than the spectral peak period, so that the spectral peak period is bound to show even larger effects of the improved numerics than the mean period T.

This paper mainly dealt with the wave model as a research tool. If a model is used as a production forecast model, the impact of errors will be different. Presently, operational wave models are mainly used to predict mean wave parameters, for which several of the preceding numerical errors partially cancel; slow growth rates are partially compensated by overestimated wave energy for low wind speeds, and effects of propagation errors in fetch-limited growth are partially compensated by indirect effects on source terms. Nevertheless, effects of numerical improvements on particular wave periods are significant. One might conclude that the majority of the effects of the improved numerics occurs for low wind speeds (with or without swell), and that consequently the old approach is a "high wind speed" approach. Note, however, that this is true only for relatively slowly varying wind fields, where a large fixed time step does not significantly influence the extreme wave heights. For hurricanes and cyclones, this need not be true. Finally, relatively new applications of wave models, such as data assimilation and the computation of ocean–atmosphere boundary-layer parameters, make a more detailed use of wave model results and are therefore potentially sensitive to effects of numerical errors.

The acceptability of numerical errors in operational models is strongly related to the economics of the numerical improvements. These economics are usually strongly influenced by the actual implementation of the model (especially on vector processors) and on the actual hardware used. For WAVEWATCH on a Cray-YMP, the extended frequency range, the dynamic time integration, and the new propagation scheme each increased the computational costs by approximately 25%, with a total increase of approximately 90%, where the simple dynamic integration method used here might leave room for improvements as discussed. Note that dynamic time integration might *save* computer time in global wave models. For instance, global WAM on a $3° \times 3°$ grid uses a propagation time step of 1 h and a source term time step of 20 min. Using dynamic integration with a basic time step of 1 h, the average source term time step might become larger than 20 min, potentially making the model cheaper.

7. Conclusions

The idealized conditions considered here show that numerical errors in the conventional third-generation approach to wind wave modeling can lead to serious misinterpretations of physics in the model. Growth rates, response to turning winds, low wind-speed behavior, swell propagation, and possibly interactions between swell and wind sea are influenced. Errors in growth rates and response to turning winds are practically eliminated by introducing dynamic time integration of source terms. Low wind-speed (and some swell/wind–sea interaction) errors can be controlled by adjusting the (high-frequency) range of the discrete spectrum. Swell propagation is improved by using improved propagation schemes. Experiments with these

numerical modification in realistic conditions show a large effect of the numerical improvements on wave periods, and a smaller, but distinct, effect on wave heights. If more detailed wind fields are used, effects on particular wave heights are expected to increase.

Acknowledgments. The author acknowledges with pleasure that Hans C. Graber generated the SWADE bottom grids used in this study and the National Meteorological Center (through SWADE) and NASA, Goddard Laboratory for Atmospheres (Dean G. Duffy) provided surface wind fields. The help of Robert Lucchesi and Joseph V. Ardizzone in visualizing and animating model results has contributed greatly to the analysis of model results. Finally the help of Dean G. Duffy, R. Wayne Higgins, and Leo H. Holthuijsen in discussing early drafts of this paper and of Laura Rumburg in preparing figures is greatly appreciated. Computer time was provided under the Air–Sea Interaction Studies Grant RTOP 461-31, funded by NASA Headquarters. This work was done while the author held a National Research Council–NASA Research Associateship.

APPENDIX

Second-Order Propagation Scheme

The method of flux-corrected transport (FCT), originally applied to the sharp and smooth transport algorithm (SHASTA), is well documented by the founding fathers of this technique (Boris and Book 1973, 1975, 1976; Book et al. 1975, 1981). Although the basic algorithm can be applied to any high-order scheme, the original approach with the SHASTA scheme is elegant for wave modeling for its relative simplicity and for the simple way in which boundary conditions can be incorporated. As is shown in the referred papers, many different SHASTA/FCT schemes can be constructed. Using the terminology introduced in the referred papers, the scheme adopted in WAVEWATCH will be defined here. For numerical formulations, terminology, and other details reference is made to these papers, in particular to Book et al. (1975) and Boris and Book (1976).

The WAVEWATCH-SHASTA scheme used here is "phoenical" (Book et al. 1975, p. 251, i.e., has no residual diffusion if the propagation velocity equals zero), except for the propagation in the physical space for spectral components that are influenced by active wave generation (defined as components with $U_{10} \cos(\theta - \theta_w)2\pi k/f > 1$). The flux limiter is that of Zalesak (1979), using both the old spectra and the propagated and diffused spectra. The limiter checks for minima only to avoid the problem of "clipping" of maxima. The propagation in the two-dimensional physical space is performed simultaneously. Refraction, however, is

handled separately (time splitting), to assure that flux limitation due to poor resolution in the physical space does not introduce diffusion in the direction space. The major disadvantage of this scheme is that for propagation across the two-dimensional spatial grid at high Courant numbers, energy is contracted in the propagation direction and diffused perpendicular to this direction. In the basin runs this has no appreciable effects, because the Courant numbers are small away from the northern and southern boundaries, but in the regional model it appears to enhance the disintegration of swell spectra due to the discrete description of the frequency space ("garden sprinkler effect," Booij and Holthuijsen 1987).

REFERENCES

Booij, N., and L. H. Holthuijsen, 1987: Propagation of ocean waves in discrete spectral wave models. *J. Comput. Phys.,* **68,** 307–336.

Book, D. L., J. P. Boris, and K. Hain, 1975: Flux-corrected transport. II: Generalization of the method. *J. Comput. Phys.,* 18, 248–283.

——, ——, and S. T. Zalesak, 1981: Flux-corrected transport. *Finite-Difference Techniques for Vectorized Fluid Dynamics,* D. L. Book, Ed., Springer, 29–55.

Boris, J. P., and D. L. Book, 1973: Flux-corrected transport. I. SHASTA, a fluid transport algorithm that works. *J. Comput. Phys.,* 11, 38–69.

——, and ——, 1975: Solution of the continuity equations by the method of flux-corrected transport. *Methods Comput. Phys.,* 16, 85–129.

——, and ——, 1976: Flux-corrected transport. III. Minimal error FCT algorithms. *J. Comput. Phys.,* 20, 397–431.

Cavaleri, L., and P. Malanotte-Rizzoli, 1981: Wind-wave prediction in shallow water: Theory and applications. *J. Geophys. Res.,* **86,** 10 961–10 973.

Fletcher, C. A. J., 1988: *Computational Techniques for Fluid Dynamics, Part I and II.* Springer, 409 and 484 pp.

Gelci, R., H. Cazalé, and J. Vassal, 1956: Utilization des diagrammes de propagation à la prévision énergétique de la houle. *Bulletin d'information du comité central d'océanographie et d'études des côtes,* 8, 169–197.

——, ——, and ——, 1957: Prévision de la haule. La méthode des densités spectroangulaires. *Bulletin d'information du comité central d'océanographie et d'études des côtes,* 9, 416–435.

Hasselmann, K., and S. Hasselmann, 1985a: The wave model EXACT-NL. *Ocean wave modelling,* the SWAMP group, Plenum Press, 256 pp.

——, and ——, 1985b: Computations and parameterizations of the nonlinear energy transfer in a gravity-wave spectrum. Part I: A new method for efficient computations of the exact nonlinear transfer integral. *J. Phys. Oceanogr.,* 15, 1369–1377.

——, T. P. Barnett, E. Bouws, H. Carlson, D. E. Cartwright, K. Enke, J. A. Ewing, H. Gienapp, D. E. Hasselmann, P. Kruseman, A. Meerburg, P. Müller, D. J. Olbers, K. Richter, W. Sell, and H. Walden, 1973: Measurements of wind-wave growth and swell decay during the Joint North Sea Wave Project (JONSWAP). *Erg. Dtsch. Hydrogr. Z.,* Reihe A (8) Nr. 12, 95 pp.

Komen, G. J., S. Hasselmann, and K. Hasselmann, 1984: On the existence of a fully developed wind-sea spectrum. *J. Phys. Oceanogr.,* 14, 1271–1285.

Madsen, O. S., Y.-K. Poon, and H. C. Graber, 1988: Spectral wave attenuation by bottom friction: Theory. *Proc. 21st Int. Conf. Coastal Eng.,* Malaga, ASCE, 492–504.

Neu, W. L., and Y. S. Won, 1990: Propagation schemes for wind-wave models with finite depth and current. *Ocean Wave Mechanics, Computational Fluid Dynamics and Mathematical Modeling,* M. Rahman Ed., Computational Mechanics Publications, 947–954.

Phillips, O. M., 1985: Spectral and statistical properties of the equilibrium range in wind-generated gravity waves. *J. Fluid Mech.,* **156,** 505–531.

Pierson, W. J., and L. Moskowitz, 1964: A proposed spectral form for fully developed wind seas based on the similarity theory of S. A. Kitaigorodskii. *J. Geophys. Res.,* **69,** 5181–5190.

Snyder, R. L., F. W. Dobson, J. A. Elliott, and R. B. Long, 1981: Array measurements of atmospheric pressure fluctuations above surface gravity waves. *J. Fluid Mech.,* **102,** 1–59.

SWAMP group, 1985: *Ocean Wave Modelling.* Plenum Press, 256 pp.

SWIM group, 1985: A shallow water intercomparison of three numerical wave prediction models (SWIM). *Quart. J. Roy. Meteor. Soc.,* **111,** 1087–1112.

Tolman, H. L., 1991: A third-generation model for wind waves on slowly varying, unsteady and inhomogeneous depths and currents. *J. Phys. Oceanogr.,* **21,** 782–797.

Vledder, G. Ph. van, and S. L. Weber, 1988: Guide for the program EXACT-NL, Max-Planck-Institut für Meteorologie, Hamburg, Rep. No. 20.

WAMDI group, 1988: The WAM model—a third generation ocean wave prediction model. *J. Phys. Oceanogr.,* **18,** 1775–1810.

Weller, R. A., M. A. Donelan, M. G. Briscoe, and N. E. Huang, 1991: Riding the crest: A tale of two wave experiments. *Bull. Amer. Meteor. Soc.,* **72,** 163–183.

Zalesak, S. T., 1979: Fully multidimensional flux-corrected transport algorithms for fluids. *J. Comput. Phys.,* **31,** 335–362.